Heterogeneous Reactions of Gaseous HNO_3 and NO_2 on the Clay Minerals Kaolinite and Pyrophyllite

Megan M. Angelini, Robert J. Garrard, Sarah J. Rosen, and Ryan Z. Hinrichs*,†

Department of Chemistry, Sarah Lawrence College, Bronxville, New York 10708

Received: November 3, 2006; In Final Form: February 20, 2007

Airborne clay mineral particles have long atmospheric lifetimes due to their relatively small size. To assess their impact on trace atmospheric gases, we investigated heterogeneous reactions on prototype clay minerals. Diffuse reflectance infrared spectroscopy identified surface-adsorbed products formed from the uptake of gaseous nitric acid and nitrogen dioxide on kaolinite and pyrophyllite. For kaolinite, a 1:1 phyllosilicate, HNO_3 molecularly adsorbed onto the octahedral aluminum hydroxide and tetrahedral silicon oxide surfaces. Also detected on the aluminum hydroxide surface were irreversibly adsorbed monodentate, bidentate, bridged, and water-coordinated nitrate species as well as surface-adsorbed water. Similar adsorbed products formed during the uptake of NO_2 on kaolinite at relative humidity (RH) of 0%, and the reaction was second order with respect to reactive surface sites and 1.5 ± 0.1 for NO_2. Reactive uptake coefficients, calculated using Brunauer, Emmett, and Teller surface areas, increased from $(8.0 \pm 0.2) \times 10^{-8}$ to $(2.3 \pm 0.4) \times 10^{-7}$ for NO_2 concentrations ranging from 0.56×10^{13} to 8.8×10^{13} molecules cm^{-3}. UV−visible spectroscopy detected gaseous HONO as a product for the reaction of NO_2 on wet kaolinite. The uptake of HNO_3 on pyrophyllite, a 2:1 phyllosilicate, resulted in stronger signal for nitric acid molecularly adsorbed on the silicon oxide surface compared to kaolinite. Monodentate, bridged, and water-coordinated nitrate species bound to aluminum sites also formed during this reaction indicating that reactive sites on edge facets are important for this system. The uptake of NO_2 on pyrophyllite, $\gamma_{BET} = (7 \pm 1) \times 10^{-9}$, was significantly lower than kaolinite because NO_2 did not react with the dominant tetrahedral silicon oxide surface. These results highlight general trends regarding the reactivity of tetrahedral silicon oxide and octahedral aluminum hydroxide clay surfaces and indicate that the heterogeneous chemistry of clay aerosols varies with mineralogy and cannot be predicted by elemental analysis.

1. Introduction

Airborne mineral dust impacts tropospheric photochemical cycles by providing reactive surface sites for heterogeneous reactions and by altering photolysis rates by scattering or absorbing solar radiation.[1−4] A global modeling study by Bian and Zender found the former to be the dominant mineral factor perturbing global O_3 and OH burdens, with heterogeneous uptake accounting for a 0.9% decrease in O_3 and a 5.1% decrease in H_xO_y.[2] Bauer and co-workers predicted that heterogeneous reactions on mineral dust were responsible for a 5% decrease in global tropospheric ozone, due primarily to the irreversible uptake of HNO_3 on mineral aerosols.[3] In this study, African dust emissions over the tropical Atlantic were predicted to have the largest regional effect, decreasing ozone levels by 10−20%.[3] East Asia also experiences intense dust storms. A study by Tang et al. simulated a 20% decline in near-surface ozone and a 95% decrease in nitric acid levels in this region.[4] Although the direct uptake of O_3 on dust does not affect global ozone levels significantly, this reaction may become important during dust storms.[3,4]

These atmospheric models, however, treat mineral dust as a single component despite regional variations in mineral aerosol composition due to differences in source region soil mineralogy.[5] Laboratory experiments routinely demonstrate that mineral composition affects heterogeneous reactions and their corresponding uptake coefficients.[6,7] This suggests that including such mineral distinctions in atmospheric models might improve accuracy, especially on a regional scale. Long-range transport also affects the composition of airborne dust clouds through mineral fractionation which occurs as large-diameter particles, often quartz and carbonate minerals, experience faster rates of gravitational settling compared to fine-grained micas and clays.[8,9] Therefore, while coarse-mode minerals impact regional atmospheres, small grain size particles (diameter $< 2\ \mu m$) such as clays are expected to have a more global impact since they comprise an increasing fraction of mineral aerosols undergoing long-range transport.

The term "clays" is commonly used to describe a broad group of aluminum phyllosilicate minerals which are formed primarily through the chemical weathering of silicate rocks. Clay particles are generally fine-mode, often having hexagonal platelet structures due to their layered silicate crystal structure.[10] Airborne clay components consist of individual platelets, aggregates of platelets, and platelets coating larger quartz particles.[8,11] Wind tunnel experiments suggest that composite particles may be fractured by impactions at high wind velocity, introducing the potential to increase the number of individual platelets suspended in the atmosphere.[12] Clay minerals are an important constituent of mineral aerosols emitted from most major arid source regions.[8] For instance, African dust measured

* To whom correspondence should be addressed. Phone: (914) 395-2392. Fax: (914) 395-2662. E-mail: rhinrichs@slc.edu.

† Address after September 2007: rhinrich@drew.edu; Drew University, Madison, NJ 07940.

10.1021/jp0672656 CCC: $37.00
Published on Web 04/06/2007

in Spain contained substantial levels of illite, smectite, palygorskite, and kaolinite, although the relative amounts varied with the source region.[13] In fact, because the relative abundance of clay components does not change with long-range transport, comparisons of individual components, such as illite-to-kaolinite ratios, provide fingerprints for identifying their region of origin.[14]

While a growing number of laboratory experiments focus on heterogeneous reactions on minerals,[6,7,15−24] only a few have considered atmospherically relevant reactions on clay minerals.[7,15−18] For instance, Hanisch and Crowley measured the uptake of gaseous nitric acid on several clay minerals using a Knudsen cell reactor.[7] After a series of experiments varying sample mass and the substrate support, these authors determined the initial uptake coefficient for nitric acid on kaolinite to be 0.114. Michel and co-workers investigated the catalytic decomposition of ozone on kaolinite, determining the initial uptake coefficient to be $(3 \pm 1) \times 10^{-5}$.[15] Interestingly, kaolinite's reactivity could not be predicted by averaging the reactivity of SiO_2 and α-Al_2O_3. Kaolinite surfaces also facilitate the conversion of adsorbed NO_3 and gaseous NO_2 into N_2O_5, which, in the presence of adsorbed water, hydrolyzes to HNO_3.[17] Mashburn et al. investigated the impact of relative humidity (RH) on the uptake of nitric acid on sodium-montmorillonite, a clay mineral that swells with increased water adsorption.[18] No adsorbed nitrate products were detected at RH = 16%, but water-coordinated nitrate was observed at RH ≥ 29%. These observations indicated that the significant uptake of HNO_3 did not occur until adsorbed water penetrated between aluminum silicate layers.[18]

The investigations described below focus on spectroscopic studies of heterogeneous reactions between gaseous nitric acid and nitrogen dioxide on kaolinite and pyrophyllite. Although there are a wide variety of clay minerals, most possess surfaces that fall into two categories: hydrophobic tetrahedral silicon oxide surfaces and hydrophilic octahedral hydroxide surfaces. Kaolinite, a 1:1 phyllosilicate $Al_2Si_2O_5(OH)_4$, consists of neutral layers containing one octahedral aluminum hydroxide sheet bonded to one tetrahedral silicon oxide sheet through a plane of shared oxygen atoms.[25] Hydrogen bonds bind adjacent layers as they stack together to form the bulk structure of kaolinite. Thus, kaolinite contains equal areas of the two surface types. Pyrophyllite, a 2:1 phyllosilicate $AlSi_2O_5OH$, is comprised of an octahedral aluminum hydroxide sheet sandwiched between two tetrahedral silicon oxide sheets. No hydroxyl groups are found on the silicon oxide surface, so dispersion forces dominate interlayer binding. Both kaolinite and pyrophyllite consist of neutral layers and do not contain interlayer cations. Therefore, these clay minerals serve as prototypes for investigating the surface chemistry of the aluminum phyllosilicate layers. Understanding how the presence of hydroxyl groups on the aluminum hydroxide surface and their absence on the silicon oxide surface affects the heterogeneous reactions with atmospheric gases will offer insight into the reactivity of many clay minerals.

2. Experimental Section

Diffuse reflectance infrared Fourier transform spectroscopy (DRIFTS) provides spectral signatures for adsorbed products formed on clay minerals during the reactive uptake of gaseous HNO_3 and NO_2. Ball-milled clay mineral powders were packed in a DRIFTS reaction chamber (Harrick Praying Mantis) using the technique described by TeVrucht and Griffiths,[26] and infrared spectra were recorded using a Thermo Nicolet 6700 FTIR equipped with a liquid-nitrogen-cooled MCT detector. A thermocouple-controlled heater allowed the temperature of the mineral sample holder to range from 298 to above 573 K. Figure 1 shows a schematic of the gas manifold setup used to continuously flow carrier and reactant gases through the DRIFTS reaction chamber. A needle-valve/flow meter (Matheson) controlled the flow of dry nitrogen carrier gas (TechAir, ultrahigh purity (UHP)), while a capacitance manometer (BOC Edwards, Barocel 600) measured the total pressure in the reaction chamber. The carrier gas flowed through the mineral powder and exited the chamber through a mesh screen and port beneath the sample holder. A second needle-valve/flow meter allowed "wet" nitrogen gas, which passed through a fritted bubbler containing deionized water (>18 MΩ), to be incrementally added to the dry N_2 flow, therefore providing control over the relative humidity of the carrier gas. A RH gauge (Vaisala, HMT 338) measured the water vapor content for the gas flow exiting the reaction chamber. A needle-valve located downstream of the RH gauge controlled the pumping rate for the carrier gas flow.

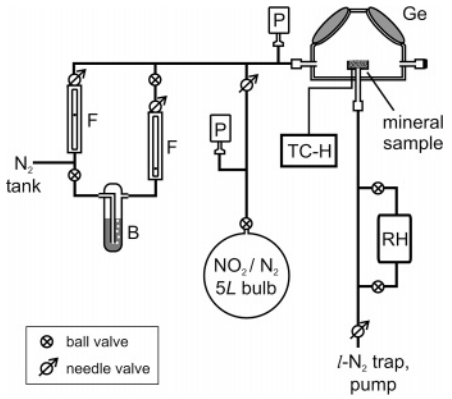

Figure 1. Schematic of DRIFTS reaction chamber and continuous flow manifold. F denotes flow meter; B, water bubbler; P, capacitance manometer; TC-H, thermocouple-controlled heater; RH, relative humidity gauge; and Ge, germanium windows.

Reactant gases (HNO_3 or NO_2) were diluted with UHP N_2 in 5 L glass bulbs with mole fractions ranging from 0.005 to 0.02. A one-to-one mixture of concentrated H_2SO_4 and HNO_3 (Aldrich) generated gaseous HNO_3. Freeze−pump−thaw cycles removed potential impurities from the NO_2 (Aldrich, 99.5%). Reactant gas mixtures entered the N_2 carrier flow through a third needle-valve upstream of the reaction chamber. A second capacitance manometer measured the pressure drop of the reactant gas mixture, allowing its flow rate to be determined. The HNO_3 (NO_2) concentration in the reaction chamber, which was constant for the duration of an experiment due to the continuous flow setup, was determined using the carrier and reactant mixture flow rates, the mixture mole fraction, and the total pressure in the reaction chamber (typically 300 Torr). Under these conditions the residence time of reactant gases in the chamber was 5 s. To minimize reactions between HNO_3 (NO_2) and the walls of the manifold and chamber, all tubing was Teflon, all stainless-steel surfaces were coated with halocarbon wax (Halocarbon Products Corp.), and germanium windows were used in the reaction chamber. A liquid nitrogen trap condensed residual HNO_3 (NO_2) upstream of the vacuum pump, and trapped NO_2 was bubbled through a triethanolamine (Sigma, 95%) and Brij 35 P (Fluka) solution for safe disposal.

Brunauer, Emmett, and Teller (BET) analysis of N_2 adsorption isotherms at 77K (Quantachrome Nova 2000e) determined surface areas for degassed mineral samples. Kaolinite powder (Aldrich) that was ball-milled for 1 min (Wig-L-Bug) had surface areas of ∼16 $m^2\ g^{-1}$. Pyrophyllite mineral (Mineralogi-

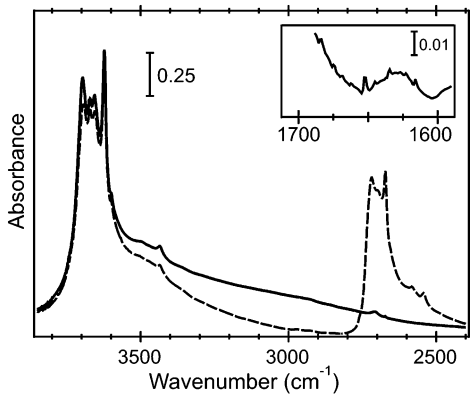

Figure 2. DRIFTS spectra of baked kaolinite powder (solid line) and partially deuterated kaolinite (dashed line). Inset shows absorbance for bending vibration of adsorbed water.

cal Research Co.) was pulverized using a mortar and pestle and then ball-milled for 3 min. Pyrophyllite surface areas were ~11 $m^2\ g^{-1}$. Approximately 100 mg of mineral were used for each DRIFTS experiment. After exposure to HNO_3 (NO_2), all reacted mineral samples were sonicated in deionized water for 1 h, and the resultant solutions were analyzed using ion chromatography (Dionex ICS-1000, AG18 column).

Separate experiments used UV−visible spectroscopy (Ocean-Optics HR2000GC-UV−near-IR with a DH2000 light source) to monitor the gas phase for the reaction of NO_2 on kaolinite. A 100 mg amount of kaolinite powder layered the bottom of a 10 cm cuvette, which was attached to a vacuum manifold. Surface-adsorbed water was added to the kaolinite by wetting the powder with deionized water and then pumping on the sample for 1 min. The addition of NO_2 diluted with UHP N_2 to the cuvette initiated the reaction. Because UV light dissociates nitrous acid (HONO), a potential gaseous product, the reaction proceeded in the dark and absorption spectra were only recorded after several minutes. Control experiments consisted of exposing a wetted, clean quartz cuvette without kaolinite to NO_2.

3. Results and Discussion

3.1. Water Adsorption. At the beginning of each experiment, clay samples were heated to 573 K for at least 2 h while purging with dry nitrogen gas to remove surface-adsorbed water. Diffuse reflectance infrared spectra of baked kaolinite samples are shown in Figure 2. Four sharp absorbance bands correspond to O−H stretching vibrations for hydroxyl groups in the octahedral aluminum hydroxide sheet: in-phase symmetric stretching vibration at 3696 cm^{-1}, two out-of-plane stretching vibrations at 3672 and 3656 cm^{-1}, and a strong absorption band at 3623 cm^{-1} associated with inner hydroxyl groups.[27] For comparison, a partially deuterated kaolinite sample, which was prepared by exposing kaolinite to D_2O vapor prior to baking, is also included in Figure 2. Deuterated hydroxyl vibrations absorbed infrared radiation at 2718, 2697, and 2672 cm^{-1} corresponding to the in-phase vibration, one out-of-plane stretching vibration, and stretching vibrations associated with the inner hydroxyl groups, respectively. The inset in Figure 2 shows the spectrum in the region of the adsorbed water bending vibration, indicating that some water (estimated to be <2% of a monolayer) remained on the minerals after baking. The origin of the minor absorbance at 3435 cm^{-1} is unknown.

Baked kaolinite was then exposed to increasing amounts of water vapor by adjusting the relative flows of dry and "wet" nitrogen. Spectra of surface-adsorbed water were recorded against the baked kaolinite spectrum as the background; thus positive absorption bands correlated with new surface species, while negative peaks corresponded to the removal of species. DRIFTS spectra were recorded after the RH of the carrier gas exiting the chamber stabilized for several minutes, indicating that water adsorption had equilibrated. Broad absorption bands ranging from 3590 to 2000 cm^{-1} increased in intensity with increasing RH (Figure 3). These features are characteristic of increased hydrogen bonding of surface hydroxyl groups to adsorbed water.[28,29] Typically, a decrease in the sharp OH absorption bands is observed concurrent with this broad band; however, absorbance data between 3725 and 3590 cm^{-1} was unreliable due to the intense absorptions described above. A second narrower (70 cm^{-1} full width at half-maximum (fwhm)) absorption band centered at 1633 cm^{-1}, which has been assigned to the bending mode vibration of surface-adsorbed water, also grew with increasing RH.

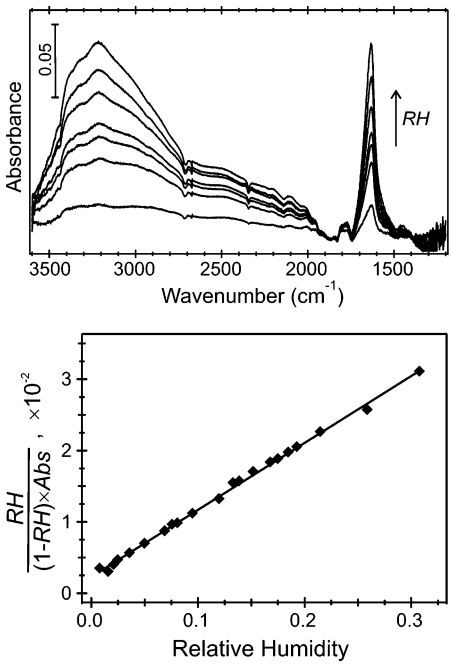

Figure 3. (a) Spectra for surface-adsorbed water recorded at RH = 0.8, 2.1, 3.6, 5.0, 9.5, 19.3, and 30.8%. (b) Linear BET plot of water adsorption isotherm for kaolinite indicating that a monolayer formed at 13% RH.

The bending mode absorption band for each spectrum was integrated between 1740 and 1480 cm^{-1}, and these values were plotted against RH to produce water adsorption isotherms. The equilibrium adsorption theory derived by Brunauer, Emmet, and Teller models adsorption isotherms assuming the potential to form an infinite number of adsorbed layers. BET theory has often been employed to analyze water adsorption on mineral surfaces as a function of relative humidity using[30]

$$V = \frac{V_m c \mathrm{RH}}{(1 - \mathrm{RH})[1 + (c - 1)\mathrm{RH}]} \qquad \text{(E1)}$$

Here V represents the volume of adsorbed water, V_m the volume of a monolayer of water, and c the ratio of the equilibrium constant for adsorption of the first layer to the equilibrium constant for all subsequent layers. Therefore, the value c also

TABLE 1: BET Parameters for Water Adsorption Isotherms

sample	c	$RH_{monolayer}$
kaolinite	42 ± 4	0.13
reacted kaolinite	27 ± 3	0.16
pyrophyllite	18 ± 5	0.19
reacted pyrophyllite	8 ± 3	0.26

relates to the relative difference in the binding energy for adsorption of the first layer, ΔH_1, versus all subsequent layers, ΔH_2:

$$c = \exp\left(\frac{\Delta H_2^\circ - \Delta H_1^\circ}{RT}\right) \quad \text{(E2)}$$

Figure 3 shows isotherm data for water adsorption on kaolinite plotted in the linear form of E1. This analysis assumed that the integrated absorbance of the water bending mode vibration was linearly proportional to the volume of adsorbed water. Although Kubelka−Munk units are traditionally used for diffuse reflectance spectroscopy,[31] work by Vogt and Finlayson-Pitts found absorbance to be linearly correlated with concentration for adsorbed products on sodium chloride powders.[32] Furthermore, a similar water adsorption isotherm plot using integrated Kubelka−Munk values was not linear. The isotherm in Figure 3 determined the equivalent of a monolayer was formed at RH = 13%, calibrating the infrared spectra of surface-adsorbed water (Table 1). Similar isotherms and results were obtained by integrating the OH stretching vibrations; we focused on the bending mode vibration due to its proximity to the nitrate vibrations discussed below.

Hydroxyl groups in pyrophyllite are only found in the inner aluminum sheet, which is sandwiched between two tetrahedral silicon oxide sheets. Pyrophyllite's baked spectrum showed only one strong OH absorption band centered at 3677 cm^{-1}. The spectra for surface-adsorbed water on pyrophyllite were similar to those recorded for kaolinite: a broad band associated with hydrogen-bonded OH stretches and the bending mode vibrational band increased with RH. BET analysis found that the equivalent of a monolayer formed at RH = 19%, indicating that the water−surface interactions were stronger for kaolinite compared to pyrophyllite. The structure of pyrophyllite requires that the main adsorption sites be located on the tetrahedral silicon oxide surface, whereas adsorption on kaolinite may also occur on the octahedral aluminum hydroxide surface. Tunega et al. classified the tetrahedral surface as hydrophobic with an adsorption energy for a single water molecule on this surface to be −4.1 kcal mol^{-1}.[33] In contrast, the adsorption energy for a single water molecule on the octahedral aluminum hydroxide surface was −14.7 kcal mol^{-1} due to stronger hydrogen bonding interactions with the surface. Our results are consistent with these calculations.

3.2. Reactions with HNO_3. Baked clay minerals were reacted with gaseous nitric acid under constant-concentration conditions at RH = 0% and 298 K. The concentration of gaseous nitric acid for these experiments ranged from 1×10^{13} to 8×10^{13} molecules cm^{-3}. DRIFTS reaction spectra, recorded against the baked mineral spectrum as a background (2 cm^{-1} resolution), monitored the production of surface-adsorbed species for these heterogeneous reactions. Each reaction spectrum was the average of 256 scans and was recorded every 3 min to monitor the relative rates at which individual absorption bands grew. Figure 4 shows a sample spectrum between 2000 and 1200 cm^{-1} for the uptake of nitric acid on kaolinite and pyrophyllite. For each mineral, these absorptions initially grew in rapidly but approached a saturation level within 200 min. The primary goal for these experiments was to identify the surface species associated with each infrared absorption band.

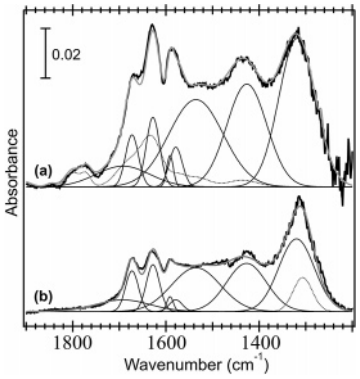

Figure 4. Reaction spectra for the uptake of nitric acid on (a) kaolinite and (b) pyrophyllite recorded at 200 min. All spectra were analyzed using a Gaussian peak-fitting procedure (see text for details). Dotted line in (a) depicts contribution from surface-adsorbed water, which was included in the total fit. Dotted line in (b) highlights additional Gaussian required to fit pyrophyllite data, which has been assigned to HNO_3 adsorbed on the silicon oxide surface.

TABLE 2: Vibrational Assignments for Water and Nitrates Adsorbed on Kaolinite and Pyrophyllite

vibrational assignment	peak position[a] (cm^{-1})
HNO_3(ads), Si and Al surfaces	1673 ± 6
bridged NO_3^-, Al site	1628 ± 4, *1319 ± 10*
H_2O(ads) bending mode	1633 ± 4
defect site NO_3^-	1591 ± 4
bidentate NO_3^-, Al site	1579 ± 3, *1319 ± 10*
monodentate NO_3^-, Al site	1535 ± 10, *1319 ± 10*
water-coordinated NO_3^-	1430 ± 10
HNO_3(ads), Si surface	1306 ± 10

[a] Uncertainties for each peak were estimated by analyzing the residual between fit and data while holding all other peak positions fixed. Italics highlight the Gaussian peak that has contributions from low-energy ν_3 absorbance bands associated with multiple aluminum bound nitrate species.

A Gaussian peak fitting procedure provided a better understanding of the complex absorbance signals in this region. Gaussian center and width parameters were optimized by fitting several reaction and postreaction (e.g., after purging, after heating) spectra simultaneously. Once these parameters were determined, all spectra were fit reasonably well, allowing only the intensities of each peak to vary. For the reaction of nitric acid on kaolinite, this peak fitting procedure identified seven significant absorption bands associated with nitrate or nitric acid vibrations (Table 2). The first significant band, centered at 1673 cm^{-1}, was assigned to molecularly adsorbed nitric acid.[23] Consistent with this assignment was the observation that this feature decreased in intensity, eventually disappearing when the reacted mineral was purged with dry nitrogen, as expected for weakly bound surface species. It is also expected that the symmetric N−O stretch for nitric acid molecularly adsorbed on the silicon oxide surface will absorb around 1310 cm^{-1},[21] and indeed a minor decrease in intensity was also observed in this region when the reacted sample was purged with dry nitrogen. No other absorbance bands decreased upon purging with nitrogen at 298 K.

Strong bands at 1628, 1579, and 1535 cm^{-1} correspond, respectively, to the high-energy ν_3 bands for bridged, bidentate, and monodentate coordinated nitrate on the aluminum hydroxide surface.[20,21,34] The low-energy ν_3 bands for these three species all absorb around 1319 cm^{-1}.[34] Although nitric acid also

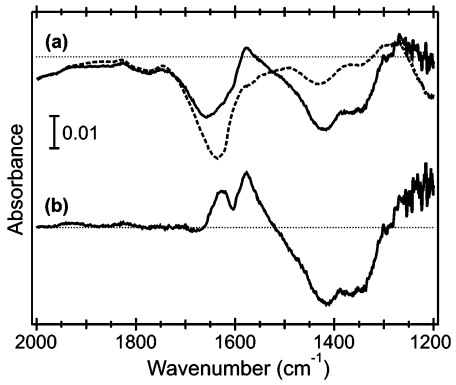

Figure 5. (a) Difference spectrum (solid line) showing absorbances of species removed when reacted kaolinite powder was heated to 373 K. Comparison to inverted spectrum for surface-adsorbed water (dashed line) indicates this was major species driven off by heating. (b) After removing the contribution from water, bottom spectrum shows surface species that increased upon heating as positive peaks while negative peaks show removed products.

absorbed in this region, the dominant signal was associated with nitrate. Absorbance bands near 1430 cm^{-1} have previously been attributed to water-coordinated nitrate ions.[18,19] The kinetics of all absorption bands discussed thus far could not be distinguished from one another; however, a minor absorption at 1591 cm^{-1} grew in intensity at a higher rate compared to the other peaks (discussed below). We therefore assign this absorption band to nitrate bound to a surface defect site or a reactive site located on the edge of the kaolinite layers.

Strong absorptions between 3500 and 2000 cm^{-1}, as well as a minor peak centered at 1780 cm^{-1}, were similar to the spectra recorded for the water adsorption isotherm. It is therefore expected that a band at 1633 cm^{-1}, associated with the bending mode vibration of surface-adsorbed water, is also present in the spectral region discussed above (dotted line in Figure 4a). This was further corroborated by changes in the spectra as a result of heating the reacted kaolinite sample to 373 K for 20 min. Figure 5a depicts species removed during heating as negative peaks, while positive peaks correspond to species that were generated during heating. This spectrum was produced by subtracting the spectrum recorded prior to heating from that recorded after heating. For comparison, the spectrum of surface-adsorbed water recorded at RH = 0.8% is included in Figure 5a (dashed line), although it has been inverted to simulate the removal of water. This combined evidence indicated that surface-adsorbed water was a product from the reaction of nitric acid on kaolinite, consistent with

$$Al{-}OH + HNO_3(ads) \rightarrow Al{-}ONO_2 + H_2O(ads) \quad (R1)$$

This reaction explains the intense monodentate nitrate signal, while the formation of surface-adsorbed water also explains the presence of water-coordinated nitrate.

Thus, adsorbed water was a major species removed when the reacted sample was heated to 373 K. To better analyze the other spectral changes associated with heating the reacted kaolinite, the contribution from water was removed from the difference spectrum producing the spectrum included in Figure 5b. Again, positive peaks correspond to absorbances that grew in intensity during heating, while negative peaks correspond to the removal of surface species. Removing surface-adsorbed water correlated with the formation of additional bridged and bidentate coordinated nitrates concurrent with a decrease of monodentate and water-coordinated nitrates.

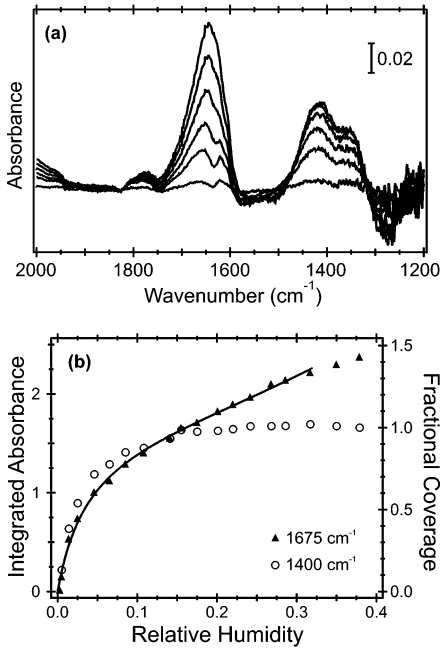

Figure 6. (a) Spectra of adsorbed water on reacted and subsequently heated kaolinite recorded at RH = 0.5, 2.5, 6.5, 14.1, 24.2, and 37.9%. (b) Adsorption isotherms integrated around 1675 cm^{-1} (adsorbed water) and 1400 cm^{-1} (water-coordinated nitrate) plotted against relative humidity; solid line generated by BET theory.

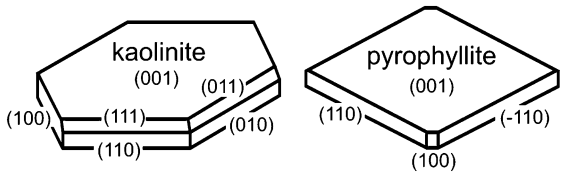

Figure 7. Schematic of well-crystallized kaolinite and pyrophyllite platelets. See refs 35 and 36 for details.

Figure 6a illustrates the results of adding surface-adsorbed water to the reacted and subsequently heated kaolinite, demonstrating that the process of removing water as shown in Figure 5 was reversible. Integrating the adsorbed water bending vibration between 1740 and 1675 cm^{-1} produced a water adsorption isotherm for reacted kaolinite; the truncated integration range ensured that artifacts associated with the decrease of the vibrational band centered at 1628 cm^{-1} were avoided. To verify that this truncated integration was valid, water adsorption isotherms discussed in the previous section were also integrated over this same region and compared to isotherms generated by integrating the entire band. This analysis for water adsorption on reacted kaolinite indicated that the equivalent of a monolayer of water formed around RH = 16% (Table 1). The integrated area of the water-coordinated nitrate band at 1430 cm^{-1}, which has been arbitrarily scaled, is also plotted against RH in Figure 6b. The formation of water-coordinated nitrate reached saturation around RH = 16%, corresponding to the formation of a monolayer of adsorbed water.

Well-crystallized kaolinite forms hexagonal platelets with diameters roughly eight times their thickness,[10] and the majority of exposed surface will correspond to the (001) plane (Figure 7).[35] It is therefore expected that the dominant monodentate, bidentate, and bridged nitrate ions are located on a relatively defect free (001) aluminum hydroxide surface. The formation of monodentate requires the displacement of one hydroxyl group (R1), while bidentate and bridged nitrate structures require the displacement of two hydroxyl groups. To maintain charge

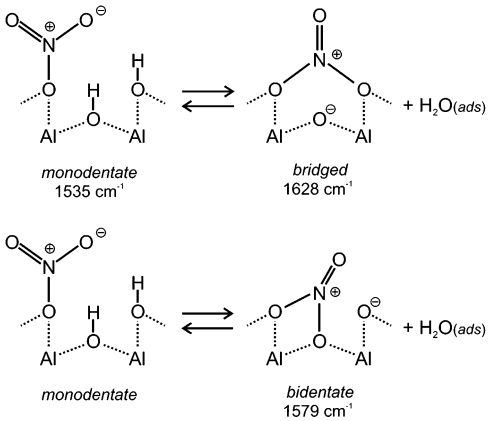

Figure 8. Proposed equilibria between monodentate nitrate and bridged (a) and bidentate (b) nitrate on the (001) octahedral aluminum hydroxide surface of kaolinite. All hydroxide groups in the octahedral aluminum sheet are coordinated to two aluminum ions; dashed lines are used to emphasize a bond order of 0.5 between each Al and O.

balance, we propose that formation of these species required deprotonation of adjacent hydroxyl groups, resulting in the production of additional surface-adsorbed water (Figure 8). These equilibrium reactions are consistent with the observations described above: removing surface-adsorbed water by heating the sample drove the equilibria in Figure 8 toward the product side, while adding surface-adsorbed water shifted the equilibria back toward reactants.

To quantify the concentration of adsorbed nitrate for the reaction-saturated kaolinite, the reacted minerals were sonicated in deionized water and analyzed using ion chromatography. The total nitrate ion count was divided by the BET surface area finding nitrate ion concentrations to range from 8.0×10^{17} to 2.1×10^{18} ions m^{-2}. Although these values were calculated using the entire BET surface area, it is likely that the nitrate ions were disproportionately located on the octahedral aluminum hydroxide sheet. These values are in good agreement with similar measurements for alumina: Underwood et al.[19] found $(1.2-2) \times 10^{18}$ ions m^{-2}, and Börensen et al.[20] measured 2.3×10^{18} ions m^{-2}.

The concentration of surface-adsorbed water can be estimated by comparing the difference spectrum in Figure 5a to the RH = 0.8% water adsorption spectrum, which was calibrated through BET analysis of the water adsorption isotherm. Approximately 19% of a monolayer of adsorbed water was detected for these experiments. The concentration of water molecules associated with a monolayer can be estimated using the molecular dynamics simulations of Tunega and co-workers,[33] in which they found nine water molecules adsorbed on the unit cell of the octahedral aluminum hydroxide surface and ten on the unit cell of the tetrahedral silicon oxide surface. Using the experimental unit cell parameters,[25] this corresponds to a concentration of 1.0×10^{19} molecules m^{-2} associated with a monolayer. Thus, we estimate that the concentration of adsorbed water molecules formed in this reaction to be $(2 \pm 2) \times 10^{18}$ molecules m^{-2}, suggesting an approximate one-to-one stoichiometry for nitrate and water. This seems low considering the proposed equilibria for formation of bidentate and bridged ions; however, this value only provides a lower limit as it was possible for water to desorb during the experiment.

Spectra recorded for the reaction of nitric acid on pyrophyllite displayed many characteristics similar to kaolinite. Therefore, these reaction spectra were fit using the same Gaussian parameters, holding peak centers and widths constant, as were optimized for kaolinite. One additional Gaussian, centered at 1306 cm^{-1}, was required to adequately fit all pyrophyllite reaction spectra (dotted line, Figure 4b). This additional peak was located in the same region as the minor decrease observed when reacted kaolinite was purged with nitrogen, which was assigned to nitric acid adsorbed on the tetrahedral silicon oxide surface. This feature was therefore not unique to pyrophyllite, but it was considerably more intense as would be expected given the prevalence of the tetrahedral silicon oxide surface for this mineral.

The dominant (001) surface for pyrophyllite crystals (Figure 7) does not contain aluminum surface sites. Therefore, detection of aluminum bound nitrate species on pyrophyllite demonstrates the importance of reactive surface sites located on edge facets, for example the (110) surface. Monodentate and water-coordinated nitrates were the dominant ionic species. A significant signal was also detected for bridged nitrate, but interestingly only a very weak signal was observed for bidentate coordinated nitrate ions. The minor peak centered at 1591 cm^{-1}, which was assigned to edge site bound nitrate for kaolinite, was also significant for pyrophyllite. Indeed, its signal was stronger than that for bidentate nitrate. Although the 1591 cm^{-1} peak displayed different kinetics than all other bands for kaolinite, it grew at a rate similar to those of the monodentate, water-coordinated, and bridged nitrate absorptions for pyrophyllite, supporting the conclusion that these species formed on the layer edge facets. Ab initio calculations identified several reactive sites on edge facets, and particular attention should be paid to the (110) and (−110) planes which are expected to be significant for pyrophyllite crystals (Figure 7).[36] In particular, Al−O−Si sites are predicted to have the highest proton affinity on the (110) surface and therefore may be important for the reaction with nitric acid.[36] The two bands associated with molecularly adsorbed nitric acid (1673 and 1306 cm^{-1}) on the (001) surface displayed different kinetics compared to the aluminum bound nitrate species. The total irreversibly adsorbed nitrate concentration was approximately $(3 \pm 2) \times 10^{17}$ ions m^{-2}, less than that measured for kaolinite.

Mashburn and co-workers[18] monitored the uptake of HNO_3 on sodium-montmorillonite as a function of RH using IR spectroscopy. The surface structure of sodium-montmorillonite is similar to pyrophyllite. However, pyrophyllite layers are neutral, while montmorillonite layers are negatively charged due to isomorphic substitutions. To maintain charge balance, montmorillonite minerals incorporate positive ions between layers, giving rise to the potential for swelling. At 40% RH, Mashburn et al. observed two nitrate peaks at 1310 and 1420 cm^{-1}, which were assigned to water-coordinated nitrate;[18] these are similar to the absorbance bands at 1319 and 1430 cm^{-1} for pyrophyllite consistent with similar surface structures. However, heating the reacted sodium-montmorillonite samples resulted in surface nitrate and ion coordinated nitrate, which absorbed at 1355 cm^{-1}.[18] This latter feature indicated that HNO_3 migrated between the phyllosilicate layers and coordinated with Na^+ ions once the water was removed. This process is not available for pyrophyllite, highlighting a distinction between swelling and nonswelling clay minerals.

3.3. Reactions with NO_2. Kaolinite was exposed to NO_2 concentrations ranging from 0.56×10^{13} to 8.8×10^{13} molecules cm^{-3}. Figure 9 shows a typical sequence of reaction spectra recorded for a NO_2 concentration of 1.0×10^{13} molecules cm^{-3} (the equilibrium concentration[37] of N_2O_4 for this experiment was 2.5×10^7 molecules cm^{-3}). The same spectral features noted above for nitric acid were also observed for the reaction with NO_2, although individual peak intensities as determined

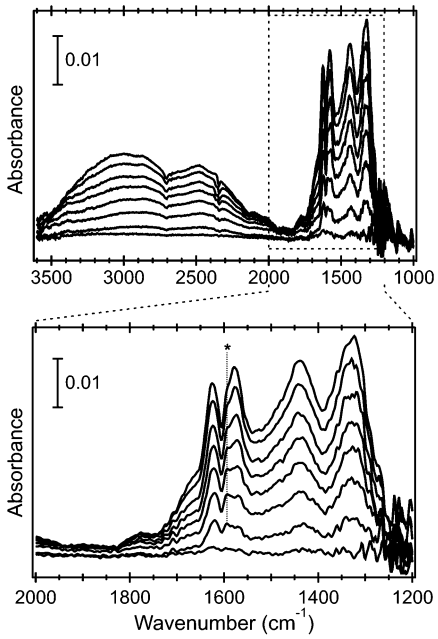

Figure 9. Reaction spectra for the uptake of NO_2 on kaolinite recorded at 3, 11, 20, 33, 51, 87, 145, and 250 min. Asterisk highlights absorbance at 1591 cm^{-1} that displayed different kinetics.

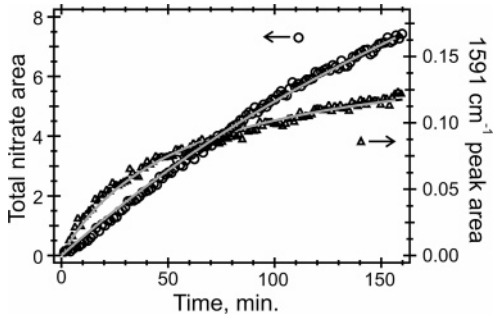

Figure 10. Plot of total nitrate area (i.e., sum of monodentate, bidentate, bridged, and water-coordinated nitrates) versus time determined by Gaussian peak-fitting procedure for 0.56×10^{13} molecules NO_2 cm^{-3}. Right axis: plot of Gaussian area for absorbance at 1591 cm^{-1}, which is attributed to nitrate on defect or edge facet surface sites.

by Gaussian fits varied. For instance, the absorbance at 1673 cm^{-1} associated with molecularly adsorbed nitric acid was substantially smaller. The relative amount of monodentate was also smaller in comparison to bridged and bidentate coordinated nitrates, possibly because the amount of surface-adsorbed water was also considerably smaller (7% of a monolayer compared to 19%). Nitrate bound to edge defects (1591 cm^{-1}) again grew at a faster rate than the other species (asterisk, Figure 9). These different kinetic behaviors are highlighted by Figure 10, which shows plots of the total nitrate Gaussian area and the 1591 cm^{-1} area versus time for kaolinite exposed to 0.56×10^{13} molecules NO_2 cm^{-3}. Total nitrate concentrations for saturated kaolinite samples were in the same range as for the reaction with nitric acid.

Although reaction rates could not be reliably measured for nitric acid due to the fast rate, kinetic measurements were performed for the uptake of NO_2 on kaolinite. Reaction spectra were integrated between 1650 and 1360 cm^{-1}, and the integrated absorbance was plotted as a function of time. To calibrate the integrated absorbance with surface nitrate concentration, several reacted kaolinite samples were analyzed using ion chromatography. The integrated absorbance varied linearly with total nitrate ion concentration, having a scaling factor of 1.4×10^{17}

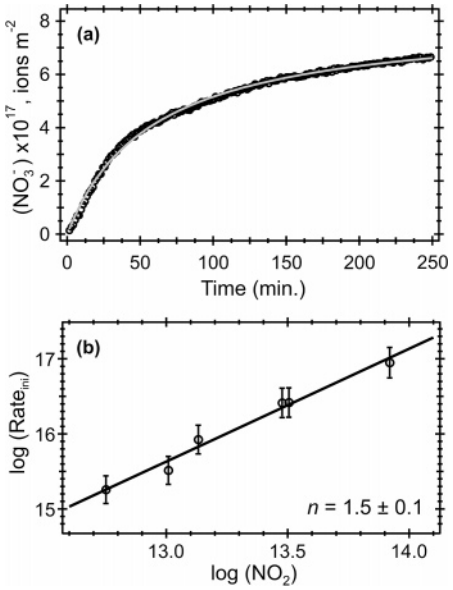

Figure 11. (a) Kinetics of adsorbed nitrate formation for $P(NO_2) = 1.0 \times 10^{13}$ molecules cm^{-3}. (b) Log−log plot to determine reaction order for NO_2.

ions m^{-2} (integrated absorbance)$^{-1}$. A sample plot of nitrate ion concentration versus time is included in Figure 11a. The empirical rate law for these reactions is expressed by

$$\text{rate} = \frac{d[NO_3^-]}{dt} = k[NO_2]^x[\text{kaolin}]^y \qquad \text{(E3)}$$

Because these experiments used a constant NO_2 concentration, the saturation of surface nitrate must correspond to a diminished availability of reactive surface sites. However, assuming the number of reactive surface sites does not change significantly during early reaction times, the initial rate should be linear. The order of reaction for NO_2 can then be determined by comparing initial rates measured for varying NO_2 concentrations using

$$\log(\text{rate}_{ini}) = \log k + x \log [NO_2] + y \log [\text{kaolin}] \qquad \text{(E4)}$$

A plot of $\log(\text{rate}_{ini})$ versus $\log [NO_2]$ was linear (Figure 11b) with a slope of 1.5 ± 0.1. Börensen and co-workers found the uptake of NO_2 on Al_2O_3 to be second order, leading them to propose a mechanism involving the disproportionation of two adsorbed NO_2 molecules forming adjacent nitrate and nitrite ions:[20]

$$2\text{Al}-\text{OH} + 2NO_2 \rightarrow \text{Al}-ONO_2 + \text{Al}-ONO + H_2O(\text{ads}) \qquad \text{(R2)}$$

Since the major nitrate products for kaolinite formed on the octahedral aluminum hydroxide surface, it is anticipated that surface hydroxyl groups will play an integral role in the reactive mechanism. No kinetic isotope effect was observed as deuterated surface hydroxyl groups reacted with rates similar to those measured for natural kaolinite.

If reaction R2 is correct, the concentration of reactive surface sites is related to the nitrate concentration via

$$0.5[\text{AlOH}]_t = [NO_3^-]_{sat.} - [NO_3^-]_t \qquad \text{(E5)}$$

where $[NO_3^-]_{sat.}$ represents the saturated nitrate concentration. Substituting this into the rate law expression and assuming the reaction was second order with respect to Al−OH yields

$$[NO_3^-]_t = [NO_3^-]_{sat.}\left(1 - \frac{1}{1 + kt[NO_3^-]_{sat.}}\right) \quad \text{(E6)}$$

This equation generated the solid line fit for the nitrate concentration versus time included in Figure 11a with a saturated nitrate concentration of $(8.2 \pm 0.5) \times 10^{17}$ ions m^{-2}. For comparison, an analogous set of equations can be derived assuming the reaction was first order with respect to surface sites. The second-order expression provided a better fit, which is confirmed by calculating the concentration of reactive surface sites using E5 (and its first-order analogue) to construct the first- and second-order rate plots shown in Figure 12. This analysis concludes that the reaction is second order with respect to surface sites. Analysis of the absorbance at 1591 cm^{-1} (Figure 10) also found defect or edge facet surface sites to follow second-order kinetics for nitrate formation. Since reaction R2 implies NO_2 adsorption on adjacent surface sites, it seems plausible that the faster kinetics for edge facets could be attributed to adjacent Al−O−Si and Al−OH_2 surface sites. Assuming these sites exhibit properties in kaolinite similar to those calculated for pyrophyllite,[36] they may enhance an electron transfer between NO_2 molecules. Further theoretical work is necessary to understand the reactivity of edge sites for this system.

Nitrite ions, which absorb around 1235 cm^{-1},[20] could not be detected in our spectroscopic experiments due to strong kaolinite lattice vibrations in this region. Nitrite ions were also not detected using ion chromatography; however, this does not eliminate a mechanism involving intermediate nitrite, which was observed for the reaction on Al_2O_3.[20] An explanation for intermediate nitrite involves its release as nitrous acid, HONO, upon protonation:

$$\text{Al}-\text{ONO} + H_2O(\text{ads}) \rightarrow \text{Al}-\text{OH} + \text{HONO(g)} \quad \text{(R3)}$$

To consider the potential release of gaseous HONO, the reaction of NO_2 on kaolinite was also studied using UV−visible spectroscopy of the gas phase. Wetted kaolinite powder was exposed to 11 Torr of NO_2 (equilibrium concentration of N_2O_4 was 1 Torr), which is considerably higher than the DRIFTS experiments but was unfortunately necessary to achieve adequate sensitivity. A sample spectrum recorded after 5 min is shown in Figure 13.

Because three nitrogen oxide species—NO_2, N_2O_4, and HONO—absorb light between 300 and 425 nm, the Abs(λ) data were analyzed using published absorbance cross-sections, $\sigma(\lambda)$,[38−40] while treating the concentration of NO_2 and HONO as variables.

$$\text{Abs}(\lambda) = [NO_2]\sigma_{NO_2}(\lambda) + [N_2O_4]\sigma_{N_2O_4}(\lambda) + [\text{HONO}]\sigma_{\text{HONO}}(\lambda) \quad \text{(E7)}$$

The NO_2 concentration determined the N_2O_4 concentration through the equilibrium expression[37]

$$2NO_2 \leftrightarrow N_2O_4 \quad \text{(R4)}$$

$$[N_2O_4] = K_{eq}[NO_2]^2 \quad \text{(E8)}$$

The resulting fits, which are included in Figure 13 as solid lines, found the HONO concentration to be $(9 \pm 1) \times 10^{15}$ molecules cm^{-3}. Analysis of spectra recorded for control experiments, performed by exposing a clean, wetted quartz cuvette to NO_2, determined that the maximum concentration of HONO from wall reaction was less than 1.2×10^{15} molecules cm^{-3}. While these results are consistent with reaction R3, it is also possible that the tetrahedral silicon oxide surface catalyzed the hydrolysis of NO_2 forming HONO. This later hypothesis is similar to the hydrolysis of NO_2 on silicon dioxide surfaces, a system which has been studied extensively.[22] Further studies are necessary to identify the mechanism (and surface) for the production of HONO on kaolinite. For example, the identification of gaseous HONO at RH = 0% would support reactions R2 and R3, indicating that the octahedral aluminum hydroxide surface was involved.

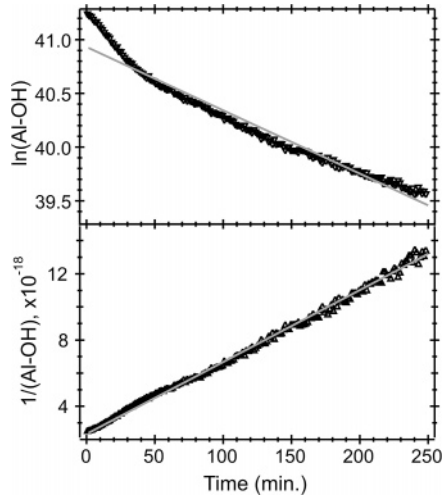

Figure 12. First-order (a) and second-order (b) rate plots for reactive surface sites for the uptake of NO_2 on kaolinite (see text for details).

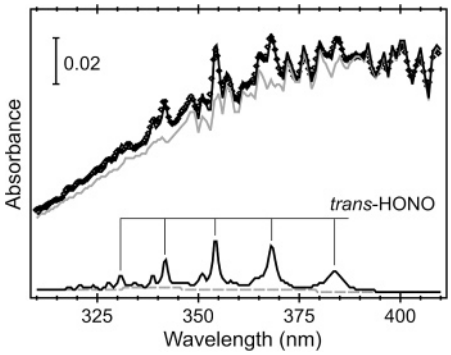

Figure 13. Gas-phase UV−visible spectrum (diamonds) for reaction of NO_2 on wetted kaolinite recorded after 5 min. Solid line fit generated by combining NO_2 (solid gray line), N_2O_4 (dashed gray line), and HONO absorbances (solid black line). HONO concentration was $(9 \pm 1) \times 10^{15}$ molecules cm^{-3}.

Reactive uptake coefficients, γ, are used to express heterogeneous reaction kinetics as the fraction of NO_2−kaolinite surface collisions that result in a reaction.

$$\gamma = \frac{d[NO_2]/dt}{Z} \quad \text{(E9)}$$

Z represents the total NO_2−kaolinite surface collision frequency as determined by the kinetic theory of gases:

$$Z = \frac{A[NO_2]}{4}\left(\frac{8RT}{\pi M_{NO_2}}\right)^{0.5} \quad \text{(E10)}$$

A is the total surface area and M_{NO_2} is the molar mass for the reactant gas. The rate of NO_2 consumption was calculated using the initial rate of nitrate formation assuming the stoichiometry of reaction R2 (Table 3). Using the BET surface area for

TABLE 3: NO_2 Kinetics on Kaolinite and Pyrophyllite at RH = 0% and 298 K

trial	$[NO_2]$ (10^{13} molecules cm^{-3})	Z^a (10^{22} molecules min^{-1})	initial rate, NO_3^- (10^{15} ions min^{-1})	γ^b
kaolinite 1	0.56	4.47	1.81 ± 0.05	$(8.1 \pm 0.2) \times 10^{-8}$
kaolinite 2	1.0	7.98	3.2 ± 0.1	$(8.0 \pm 0.3) \times 10^{-8}$
kaolinite 3	1.4	11.2	8.4 ± 0.1	$(1.5 \pm 0.3) \times 10^{-7}$
kaolinite 4	3.0	24.0	25 ± 2	$(2.1 \pm 0.3) \times 10^{-7}$
kaolinite 5	3.2	25.6	26 ± 2	$(2.0 \pm 0.3) \times 10^{-7}$
kaolinite 6	8.8	70.3	79 ± 4	$(2.3 \pm 0.4) \times 10^{-7}$
pyrophyllite	30	165	5.8 ± 0.5	$(7 \pm 1) \times 10^{-9}$

[a] Z = the collision rate. [b] γ = reactive uptake coefficient.

kaolinite, reactive uptake coefficients increased from $(8.0 \pm 0.2) \times 10^{-8}$ to $(2.3 \pm 0.4) \times 10^{-7}$ for NO_2 concentrations ranging from 0.56×10^{13} to 8.8×10^{13} molecules cm^{-3}.

Assuming the entire BET surface area for this reaction may overestimate the available surface for reaction since the kaolinite powder was packed in a sample cup, and these uptake coefficients should be considered to represent a lower limit for the actual value. While an upper limit could be determined using the geometrical surface area of the sample cup, these results (4.5×10^{-3} to 1.2×10^{-2}) seem extreme given the experimental setup, where the reactant gas flowed through the mineral powder, and the magnitude of the uptake coefficients. Li and co-workers[41] modeled the diffusion of reactant gases into powder samples for Knudsen cell experiments. When uptake coefficients are less than 10^{-4}, reactant gas diffusion was sufficiently fast that all layers contributed to the measured uptake.[41] Although our DRIFTS samples contain many more layers compared to their Knudsen cell reactor, their results further support the use of BET surface areas for NO_2 uptake. Reactive uptake coefficients for the reaction of NO_2 on alumina varied linearly from 7.3×10^{-10} to 1.3×10^{-8} for NO_2 concentrations ranging from 2.5×10^{13} to 8.5×10^{14} molecules cm^{-3}.[20] Although the adsorbed products and proposed mechanism were similar for kaolinite and alumina, kaolinite had higher uptake coefficients, indicating that the reactive surfaces for these two minerals differ. Our reactive uptake coefficients indicate that these reactions are not atmospherically important relative to NO_2 concentrations and will therefore not impact tropospheric ozone concentrations. However, in highly polluted environments where NO_2 concentrations can reach 5×10^{12} molecules cm^{-3},[42] kaolinite aerosols may acquire a 50% nitrate coating in 7 h.

The reactive uptake of nitrogen dioxide on pyrophyllite was studied at the comparatively high concentration of $[NO_2] = 30 \times 10^{13}$ molecules cm^{-3}. The Gaussian peak-fitting analysis identified the key aluminum bound nitrates species noted above, with spectral signatures at 1628 (bridged), 1579 (bidentate), 1535 (monodentate), and 1319 cm^{-1} (low-energy ν_3). Water-coordinated nitrate (1430 cm^{-1}) and molecular HNO_3 associated with aluminum hydroxide surface sites (1673 cm^{-1}) were also detected. However, the additional Gaussian at 1306 cm^{-1}, which corresponded to molecularly adsorbed nitric acid on the tetrahedral silicon oxide surface for pyrophyllite, was not needed to fit the NO_2 reaction spectra. This observation suggests that NO_2 did not react on the silicon oxide surface. Since the reactive surface sites were limited to pyrophyllite edge facets, it was not surprising that the reactive uptake coefficient for NO_2, assuming a second-order reaction, was at least an order of magnitude lower, $\gamma_{BET} = (7 \pm 1) \times 10^{-9}$, than measured for kaolinite and were also lower than the value for alumina measured at a comparable NO_2 concentration.[20]

These results support the prior observation[15] that the heterogeneous chemistry of aluminum phyllosilicate clay minerals cannot be predicted by the reactivity of alumina, Al_2O_3, and silica, SiO_2. Therefore, simple elemental analysis of atmospheric aerosols does not provide enough information to understand their reactivity; individual mineral components must be identified. Although there were similarities in the nature of the adsorbed products for clays compared to alumina and silica, there were also quantitative differences that must be attributed to characteristics of the mineral surfaces. The silicate sheet structure of clay minerals presents different surface sites compared to other minerals,[35] and general trends relating to the properties of clay mineral surfaces can begin to be articulated. In particular, tetrahedral silicon oxide surfaces, characterized by hydrophobic basal oxygens, do not react with NO_2. Meanwhile, the hydrophilic octahedral aluminum hydroxide surfaces are quite reactive and account for significant NO_2 uptake coefficients for kaolinite. Other 1:1 clay minerals in the kaolinite−serpentine group (e.g., chrysotile and lizardite) with surface hydroxyl groups are therefore expected to react with NO_2. Minerals in the chlorite group will also likely react with NO_2 since they contain positively charged octahedral hydroxide layers stacked between negatively charged 2:1 layers.

4. Conclusions

Infrared spectroscopy identified surface-adsorbed species for the heterogeneous uptake of gaseous HNO_3 and NO_2 on prototype clay minerals. Kaolinite contains two distinct surfaces—a hydrophobic tetrahedral silicon oxide surface and a hydrophilic octahedral aluminum hydroxide surface—that displayed different chemistry. The dominant surface products formed on the aluminum hydroxide surface and included monodentate, bidentate, and bridged nitrate. The reactions forming these nitrate species also produced surface-adsorbed water, which in turn allowed for the formation of water-coordinated nitrate. In contrast, the main product formed on the silicon oxide surface was molecularly adsorbed nitric acid, which was only detected in significant quantities for the reaction with gaseous nitric acid. Pyrophyllite is a 2:1 aluminum phyllosilicate whose major (001) surfaces consist of tetrahedral silicon oxide sheets, and thus molecularly adsorbed nitric acid was a major product for this mineral. However, substantial signals for monodentate and bridged nitrates indicate that edge facets, such as the (110) surface, provide reactive surface sites that affect the reactivity of clays. Edge facets were also important for kaolinite's reactivity as evidenced by the accelerated kinetics of a nitrate absorbance at 1591 cm^{-1}.

The reaction of nitrogen dioxide on kaolinite was second order with respect to reactive surface sites and had an order of 1.5 ± 0.1 for NO_2. UV−visible spectroscopy identified gaseous HONO as a product for the reaction of NO_2 on wetted kaolinite, which is significant since the photolysis of gaseous HONO acts as a major source of OH radicals in urban and rural environments.[42] Further experiments are necessary to quantify HONO formation on kaolinite. Reactive uptake coefficients for NO_2 on kaolinite ranged from $(8.0 \pm 0.2) \times 10^{-8}$ to $(2.3 \pm 0.4) \times 10^{-7}$, while the value was considerably lower for pyrophyllite,

$(7 \pm 1) \times 10^{-9}$. These results, along with the absence of a peak at 1306 cm^{-1} for pyrophyllite, suggest that NO_2 did not react on the tetrahedral silicon oxide surface. Although these reactive uptake coefficients indicate these specific reactions will not play an important role in tropospheric chemistry, they do highlight the fact that mineralogy impacts on the heterogeneous chemistry of mineral dust. Differences were noted in comparing the heterogeneous reactions on clay minerals to other mineral compounds such as silica and alumina. Therefore, the heterogeneous chemistry of airborne clay aerosols cannot be predicted by elemental analysis. Since airborne clay aerosols are expected to undergo long-range transport due to their relatively small particle size, these results highlight the need to conduct more laboratory experiments investigating atmospheric heterogeneous reactions on clay mineral surfaces.

Acknowledgment. We gratefully acknowledge the National Science Foundation (Grant ATM-0424946) for support of this research. We thank Dr. B. Finlayson-Pitts and her laboratory, especially Dr. W. Roberts, for suggestions regarding DRIFTS spectroscopy and R. W. Hempel for ion chromatography results.

References and Notes

(1) Dentener, F. J.; Carmichael, G. R.; Zhang, Y.; Lelieveld, J.; Crutzen, P. J. *J. Geophys. Res.* **1996**, *101*, 22869.

(2) Bian, H.; Zender, C. S. *J. Geophys. Res.* **2003**, *108* (D21), 4672.

(3) Bauer, S. E.; Balkanski, Y.; Schulz, M.; Hauglustaine, D. A.; Dentener, F. *J. Geophys. Res.* **2004**, *109*, D02304.

(4) Tang, Y.; Carmichael, G. R.; Kurata, G.; Uno, I.; Weber, R. J.; Song, C.-H.; Guttikunda, S. K.; Woo, J.-H.; Streets, D. G.; Wei, C.; Clarke, A. D.; Huebert, B.; Anderson, T. L. *J. Geophys. Res.* **2004**, *109*, D19S21.

(5) Claquin, T.; Schulz, M.; Balkanski, Y. J. *J. Geophys. Res.* **1999**, *104* (D18), 22243.

(6) Usher, C. R.; Michel, A. E.; Grassian, V. H. *Chem. Rev.* **2003**, *103*, 4883.

(7) Hanisch, F.; Crowley, J. N. *Phys. Chem. Chem. Phys.* **2001**, *3*, 2474.

(8) Pye, K. *Aeolian Dust and Dust Deposits*; Academic Press: London, U.K., 1987.

(9) Prospero, J. M. *Proc. Natl. Acad. Sci. U.S.A.* **1999**, *96*, 3396.

(10) Worrall, W. E. *Clays: Their Nature, Origin and General Properties*; MacLaren & Sons: London, U.K., 1968.

(11) Buseck, P. R.; Pósfai, M. *Proc. Natl. Acad. Sci. U.S.A.* **1999**, *96*, 3372.

(12) Alfaro, S. C.; Gaudichet, A.; Gomes, L.; Maillé, M. *Geophys. Res. Lett.* **1998**, *25*, 991.

(13) Avila, A.; Queralt-Mitjans, I.; Alarcón, M. *J. Geophys. Res.* **1997**, *102* (D18), 21977.

(14) Caquineau, S.; Gaudichet, A.; Gomes, L.; Legrand, M. *J. Geophys. Res.* **2002**, *107* (D15), 4251.

(15) Michel, A. E.; Usher, C. R.; Grassian, V. H. *Atmos. Environ.* **2003**, *37*, 3201.

(16) Kutsuna, S.; Takeuchi, K.; Ibusuki, T. *J. Geophys. Res.* **2000**, *105* (D5), 6611.

(17) Karagulian, F.; Rossi, M. J. *Phys. Chem. Chem. Phys.* **2005**, *7*, 3150.

(18) Mashburn, C. D.; Frinak, E. K.; Tolbert, M. A. *J. Geophys. Res.* **2006**, *111*, D15213.

(19) Underwood, G. M.; Miller, T. M.; Grassian, V. H. *J. Phys. Chem. A* **1999**, *103*, 6184.

(20) Börensen, C.; Kirchner, U.; Scheer, V.; Vogt, R.; Zellner, R. *J. Phys. Chem. A* **2000**, *104*, 5036.

(21) Goodman, A. L.; Bernard, E. T.; Grassian, V. H. *J. Phys. Chem. A* **2001**, *105*, 6443.

(22) Finlayson-Pitts, B. J.; Wingen, L. M.; Sumner, A. L.; Syomin, D.; Ramazan, K. A. *Phys. Chem. Chem. Phys.* **2003**, *5*, 223.

(23) Seisel, S.; Börensen, C.; Vogt, R.; Zellner, R. *Phys. Chem. Chem. Phys.* **2004**, *6*, 5498.

(24) Vlasenko, A.; Sjogren, S.; Weingartner, E.; Stemmler, K.; Gäggeler, H. W.; Ammann, M. *Atmos. Chem. Phys.* **2006**, *6*, 2147.

(25) Bailey, S. W. Structures of Layered Silicates. In *Crystal Structures of Clay Minerals and Their X-ray Identification*; Brindley, G. W., Brown, G., Eds.; Mineralogical Society: London, U.K., 1980.

(26) TeVrucht, M. L. E.; Griffiths, P. R. *Appl. Spectrosc.* **1989**, *43*, 1492.

(27) Madejová, J. *Vib. Spectrosc.* **2003**, *31*, 1.

(28) Little, L. H. *Infrared Spectra of Adsorbed Species*; Academic Press: London, U.K., 1966.

(29) Hair, M. L. *Infrared Spectroscopy in Surface Chemistry*; Marcel Dekker, Inc.: New York, NY, 1967.

(30) Newman, A. C. D. In *Chemistry of Clays and Clay Minerals*; Mineralogical Society Monograph No. 6; Newman, A. C. D., Ed.; Longman Scientific & Technical: Essex, U.K., 1987; Chapter 5, pp 237−274.

(31) Griffiths, P. R.; Fuller, M. P. In *Advances in Infrared and Raman Spectroscopy*, Vol. 9; Clark, R. J. H., Hester, R. E., Eds.; Heyden Publishing Co.: London, U.K., 1982; Chapter 2.

(32) Vogt, R.; Finlayson-Pitts, B. J. *J. Phys. Chem.* **1994**, *98*, 3747.

(33) Tunega, D.; Gerzabek, M. H.; Lischka, H. *J. Phys. Chem. B* **2004**, *108*, 5930.

(34) Davydov, A. *Molecular Spectroscopy of Oxide Catalyst Surfaces*; John Wiley & Sons: New York, NY, 2003.

(35) Murashov, V. V.; Demchuk, E. *J. Phys. Chem. A* **2005**, *109*, 10835.

(36) Churakov, S. V. *J. Phys. Chem. B* **2006**, *110*, 4135.

(37) Sander, S. P.; Friedl, R. R.; Golden, D. M.; Kurylo, M. J.; Huie, R. E.; Orkin, V. L.; Moortgat, G. K.; Ravishankara, A. R.; Kolb, C. E.; Molina, M. J.; Finlayson-Pitts, B. J. In *Chemical Kinetics and Photochemical Data for Use in Atmospheric Studies*, Evaluation No. 14; JPL Publication 02-25; JPL: Pasadena, CA, 2003.

(38) Harwood, M. H.; Jones, R. L. *J. Geophys. Res.* **1994**, *99* (D11), 22955.

(39) Bongartz, A.; Kames, J.; Welter, F.; Schurath, U. *J. Phys. Chem.* **1991**, *95*, 1076.

(40) Bongartz, A.; Kames, J.; Schurath, U.; George, Ch.; Mirabel, Ph.; Ponche, J. L. *J. Atmos. Chem.* **1994**, *18*, 149.

(41) Li, P.; Al-Abadleh, H. A.; Grassian, V. H. *J. Phys. Chem. A* **2002**, *106*, 1210.

(42) Finlayson-Pitts, B. J.; Pitts, J. N. *Chemistry of the Upper and Lower Atmosphere*; Academic Press: San Diego, CA, 2000.